

SUBMILLIMETER OBSERVATIONS OF MILLIMETER BRIGHT GALAXIES DISCOVERED BY THE SOUTH POLE TELESCOPE

T. R. GREVE¹, J. D. VIEIRA², A. WEIß³, J. E. AGUIRRE⁴, K. A. AIRD⁵, M. L. N. ASHBY⁶, B. A. BENSON^{7,8}, L. E. BLEEM^{7,9}, C. M. BRADFORD¹⁰, M. BRODWIN⁶, J. E. CARLSTROM^{7,8,9,11,12}, C. L. CHANG^{7,8,12}, S. C. CHAPMAN¹³, T. M. CRAWFORD^{7,11}, C. DE BREUCK¹⁴, T. DE HAAN¹⁵, M. A. DOBBS¹⁵, T. DOWNES², C. D. FASSNACHT¹⁶, G. FAZIO⁶, E. M. GEORGE¹⁷, M. GLADDERS^{7,11}, A. H. GONZALEZ¹⁸, N. W. HALVERSON¹⁹, Y. HEZAVEH¹⁵, F. W. HIGH^{7,11}, G. P. HOLDER¹⁵, W. L. HOLZAPFEL¹⁷, S. HOOVER^{7,8}, J. D. HRUBES⁵, M. JOHNSON²⁰, R. KEISLER^{7,9}, L. KNOX¹⁶, A. T. LEE^{17,21}, E. M. LEITCH^{7,11}, M. LUEKER², D. LUONG-VAN⁵, M. MALKAN²⁰, D. P. MARRONE²², V. MCINTYRE²³, J. J. McMAHON²⁴, J. MEHL⁷, K. M. MENTEN³, S. S. MEYER^{7,8,9,11}, T. MONTRY²⁵, E. J. MURPHY²⁶, T. NATOLI^{7,8}, S. PADIN^{2,7,11}, T. PLAGGE^{7,11}, C. PRYKE^{7,8,11}, C. L. REICHARDT¹⁷, A. REST^{27,28}, M. ROSENMAN⁴, J. RUEL²⁷, J. E. RUHL²⁵, K. K. SCHAFFER^{7,29}, K. SHARON⁷, L. SHAW³⁰, E. SHIROKOFF^{2,17}, B. STALDER^{6,27}, S. A. STANFORD¹⁶, Z. STANISZEWSKI^{2,25}, A. A. STARK⁶, K. STORY^{7,8}, K. VANDERLINDE¹⁵, W. WALSH⁶, N. WELIKALA³¹, AND R. WILLIAMSON^{7,11}

¹ Department of Physics and Astronomy, University College London, Gower Street, London WC1E 6BT, UK; tgreve@star.ucl.ac.uk

² California Institute of Technology, 1216 East California Boulevard, Pasadena, CA 91125, USA

³ Max-Planck-Institut für Radioastronomie, Auf dem Hügel 69, D-53121 Bonn, Germany

⁴ Department of Physics and Astronomy, University of Pennsylvania, 209 South 33rd Street, Philadelphia, PA 19104, USA

⁵ Department of Astronomy and Astrophysics, University of Chicago, 5640 South Ellis Avenue, Chicago, IL 60637, USA

⁶ Harvard-Smithsonian Center for Astrophysics, 60 Garden Street, Cambridge, MA 02138, USA

⁷ Kavli Institute for Cosmological Physics, University of Chicago, 5640 South Ellis Avenue, Chicago, IL 60637, USA

⁸ Enrico Fermi Institute, University of Chicago, 5640 South Ellis Avenue, Chicago, IL 60637, USA

⁹ Department of Physics, University of Chicago, 5640 South Ellis Avenue, Chicago, IL 60637, USA

¹⁰ Jet Propulsion Laboratory, 4800 Oak Grove Drive, Pasadena, CA 91109, USA

¹¹ Department of Astronomy and Astrophysics, University of Chicago, 5640 South Ellis Avenue, Chicago, IL 60637, USA

¹² Argonne National Laboratory, 9700 S. Cass Avenue, Argonne, IL 60439, USA

¹³ Institute of Astronomy, University of Cambridge, Madingley Road, Cambridge CB3 0HA, UK

¹⁴ European Southern Observatory, Karl-Schwarzschild Strasse, D-85748 Garching bei München, Germany

¹⁵ Department of Physics, McGill University, 3600 Rue University, Montreal, Quebec H3A 2T8, Canada

¹⁶ Department of Physics, University of California, One Shields Avenue, Davis, CA 95616, USA

¹⁷ Department of Physics, University of California, Berkeley, CA 94720, USA

¹⁸ Department of Astronomy, University of Florida, Gainesville, FL 32611, USA

¹⁹ Department of Astrophysical and Planetary Sciences and Department of Physics, University of Colorado, Boulder, CO 80309, USA

²⁰ Department of Physics and Astronomy, University of California, Los Angeles, CA 90095-1547, USA

²¹ Physics Division, Lawrence Berkeley National Laboratory, Berkeley, CA 94720, USA

²² Steward Observatory, University of Arizona, 933 North Cherry Avenue, Tucson, AZ 85721, USA

²³ Australia Telescope National Facility, CSIRO, Epping, NSW 1710, Australia

²⁴ Department of Physics, University of Michigan, 450 Church Street, Ann Arbor, MI 48109, USA

²⁵ Physics Department, Center for Education and Research in Cosmology and Astrophysics, Case Western Reserve University, Cleveland, OH 44106, USA

²⁶ Observatories of the Carnegie Institution for Science, 813 Santa Barbara Street, Pasadena, CA 91101, USA

²⁷ Department of Physics, Harvard University, 17 Oxford Street, Cambridge, MA 02138, USA

²⁸ Space Telescope Science Institute, 3700 San Martin Drive, Baltimore, MD 21218, USA

²⁹ Liberal Arts Department, School of the Art Institute of Chicago, 112 South Michigan Avenue, Chicago, IL 60603, USA

³⁰ Department of Physics, Yale University, P.O. Box 208210, New Haven, CT 06520-8120, USA

³¹ Institut d’Astrophysique Spatiale, Bâtiment 121, Université Paris-Sud XI and CNRS, 91405 Orsay Cedex, France

Received 2011 December 5; accepted 2012 June 19; published 2012 August 20

ABSTRACT

We present APEX SABOCA 350 μm and LABOCA 870 μm observations of 11 representative examples of the rare, extremely bright ($S_{1.4\text{ mm}} > 15 \text{ mJy}$), dust-dominated millimeter-selected galaxies recently discovered by the South Pole Telescope. All 11 sources are robustly detected with LABOCA with $40 \text{ mJy} < S_{870\text{ }\mu\text{m}} < 130 \text{ mJy}$, approximately an order of magnitude higher than the canonical submillimeter galaxy (SMG) population. Six of the sources are also detected by SABOCA at $>3\sigma$, with the detections or upper limits providing a key constraint on the shape of the spectral energy distribution (SED) near its peak. We model the SEDs of these galaxies using a simple modified blackbody and perform the same analysis on samples of SMGs of known redshift from the literature. These calibration samples inform the distribution of dust temperature for similar SMG populations, and this dust temperature prior allows us to derive photometric redshift estimates and far-infrared luminosities for the sources. We find a median redshift of $\bar{z} = 3.0$, higher than the $\bar{z} = 2.2$ inferred for the normal SMG population. We also derive the apparent size of the sources from the temperature and apparent luminosity, finding them to appear larger than our unlensed calibration sample, which supports the idea that these sources are gravitationally magnified by massive structures along the line of sight.

Key words: galaxies: evolution – galaxies: formation – galaxies: high-redshift – galaxies: starburst – submillimeter: galaxies

1. INTRODUCTION

The first extragalactic surveys at submillimeter (submm) wavelengths carried out at $850\text{ }\mu\text{m}$ with SCUBA (Holland et al. 1999) over a decade ago (Smail et al. 1997; Hughes et al. 1998; Barger et al. 1998) discovered a population of optically faint, submm bright galaxies. Multi-wavelength follow-up campaigns subsequently established that the bright ($S_{850\text{ }\mu\text{m}} \sim 3\text{--}15\text{ mJy}$) submillimeter galaxies (SMGs) represent a significant population of distant ($z \simeq 1\text{--}3$) dust-enshrouded, far-infrared (FIR) luminous ($L_{\text{FIR}} \sim 10^{13}\text{ }L_{\odot}$) galaxies, in which large gas reservoirs ($M(\text{H}_2) \sim 10^{11}\text{ }M_{\odot}$) are being turned into stars at a prodigious rate ($\text{SFR} \sim 1000\text{ }M_{\odot}\text{ yr}^{-1}$; e.g., Neri et al. 2003; Chapman et al. 2005).

Ground-based extragalactic surveys conducted at wavelengths of $850\text{--}1200\text{ }\mu\text{m}$ have identified a few hundred sources in total sky area of $\sim 4\text{ deg}^2$ (e.g., Coppin et al. 2006; Perera et al. 2008; Austermann et al. 2009; Weiß et al. 2009). The brightest sources found in these surveys have $S_{850\text{ }\mu\text{m}} \lesssim 20\text{ mJy}$ and a source density of $\sim 1\text{ deg}^{-2}$. A handful of brighter sources have been discovered in small area surveys by targeting massive galaxy clusters and thereby taking advantage of gravitational magnification. For example, ultra-bright SMGs have been found behind the Bullet Cluster (1ES 0657–56, $S_{870\text{ }\mu\text{m}} = 48\text{ mJy}$, $z = 2.79$; Wilson et al. 2008; Gonzalez et al. 2010; Johansson et al. 2010) and MACS J2135–010217 (SMM J2135–0102, hereafter called the “Eyelash,” $S_{870\text{ }\mu\text{m}} = 106\text{ mJy}$, $z = 2.33$; Swinbank et al. 2010; Ivison et al. 2010; Danielson et al. 2011). Sources lensed by intervening galaxies have also been found serendipitously ($S_{870\text{ }\mu\text{m}} \sim 100\text{ mJy}$, $z = 3\text{--}4$; Lestrade et al. 2010; Ikarashi et al. 2011). These objects are important as gravitationally magnified windows on the obscured star formation process in the early universe, but large samples of these rare objects cannot be obtained in surveys of a few square degrees.

The landscape of submm surveys has changed dramatically in the last few years with the advent of observatories capable of mapping large areas of sky simultaneously in multiple bands. The Balloon-borne Large-Aperture Submillimeter Telescope (BLAST; Pascale et al. 2008) mapped over 10 deg^2 at 250, 350, and $500\text{ }\mu\text{m}$ (Devlin et al. 2009), identifying many dusty galaxies and providing photometric redshift estimates. The 10 m South Pole Telescope (SPT) surveyed 200 deg^2 to mJy depth at 1.4 and 2.0 mm in 2008, discovering a population of rare ($\sim 0.1\text{ deg}^{-2}$) and extremely bright ($> 20\text{ mJy}$ at 1.4 mm) dusty galaxies (Vieira et al. 2010). Early results from the Science Demonstration Phase (SDP) observations of the *Herschel* Astrophysical Terahertz Large Area Survey (H-ATLAS; Eales et al. 2010) and the *Herschel* Multi-tiered Extragalactic Survey (HerMES; Oliver et al. 2010)—each surveying tens of deg^2 at 250, 350, and $500\text{ }\mu\text{m}$ —also identified analogous populations of bright sources (Negrello et al. 2010; Conley et al. 2011).

In this paper, we denote SMGs with $S_{850\text{ }\mu\text{m}} > 30\text{ mJy}$, primarily discovered in the large-area surveys described above, as “ultra-bright” SMGs. These sources appear more luminous than galaxies identified in smaller surveys ($S_{850\text{ }\mu\text{m}} \simeq 3\text{--}15\text{ mJy}$); we refer to the fainter, unlensed population as “normal” SMGs. The apparent luminosity of the ultra-bright SMGs, as well as their excess relative to the expected high-flux number counts of normal SMGs, is a strong indication that a significant fraction are strongly lensed with magnification factors of order 10–50 (Blain 1996; Blain et al. 1999; Negrello et al. 2007; Hezaveh & Holder 2011).

Measuring this lensing amplification—using high-resolution follow-up imaging and detailed lens modeling—is one of the keys to determining the intrinsic properties of these ultra-bright SMGs and their place in the overall scheme of galaxy evolution. The other key, which we focus on in this work, is determining their redshifts. Recent “blind” CO line searches, i.e., without prior optical/near-IR spectroscopy, with the Zpectrometer (Frayer et al. 2011) on the Green Bank Telescope and Z-Spec (Bradford et al. 2009) on the Caltech Submillimeter Observatory (CSO) yielded redshifts in the range $z \simeq 1.6\text{--}3.0$ for five ultra-bright H-ATLAS sources (Frayer et al. 2011; Lupu et al. 2010). At present, robust spectroscopic redshifts have been published for 10 such ultra-bright SMGs—discovered either from the ground or with *Herschel*—although several more sources from H-ATLAS and HerMES have now been spectroscopically confirmed (Harris et al. 2012). The bulk of these lie within the observed redshift range of normal, radio-identified SMGs ($z \sim 1\text{--}3$; Chapman et al. 2005), which may in part be due to the frequency coverage of Zpectrometer and Z-Spec favoring $z < 4$ CO detections. The redshift of the single $z > 4$ ultra-bright SMG published to date was made using the IRAM Plateau de Bure Interferometer WideX correlator (Cox et al. 2011). A large overlap between the SPT and *Herschel* sources is expected, but the longer SPT selection wavelength (1.4 mm) does predict a broader redshift range than the $350\text{--}500\text{ }\mu\text{m}$ selected *Herschel* sources. The SPT may also be sensitive to a population of cooler sources that are invisible to the shorter wavelength *Herschel* selection. The large SPT survey area (2500 deg^2 , compared to the 600 and 380 deg^2 that H-ATLAS and HerMES cover) ensures the identification of the rarest and most highly magnified objects in the sky.

In this paper, we present the first 350 and $870\text{ }\mu\text{m}$ maps of a subset of 11 SPT sources. In Section 2, the Submillimeter Apex BOlometer CAmera (SABOCA) and Large Apex BOlometer CAmera (LABOCA) observations and data reduction are outlined. In Sections 3.1 and 3.2 we describe the submm maps, source morphology, and fluxes, while in Sections 3.3 and 3.4 we fit spectral energy distributions (SEDs) and derive photometric redshifts, FIR luminosities, and dust temperatures based on the SEDs. Finally, in Section 4, we discuss the derived properties of SPT sources, including their redshifts, and the implications these findings have. Throughout, we adopt a flat cosmology with $\Omega_M = 0.27$, $\Omega_\Lambda = 0.73$, and $h = 0.71$ (Spergel et al. 2003).

2. OBSERVATIONS AND DATA REDUCTION

2.1. South Pole Telescope Selection

The SPT (Carlstrom et al. 2011), a 10 m off-axis Gregorian design with a 1 deg^2 field of view, has been surveying the mm-wave sky with unprecedented sensitivity and angular resolution since its commissioning in 2007. The SPT is located within 1 km of the geographical South Pole. At an altitude of 2800 m above sea level, the South Pole is one of the premier locations for mm-wave astronomy. The high altitude and low temperatures ensure an atmosphere with low water-vapor content and excellent transparency. Meanwhile, the location at the Earth’s rotational axis allows 24 hr access to the target fields.

The first receiver mounted on the SPT is a camera consisting of 840 transition-edge-sensor (TES) bolometers, optimized for fine-scale anisotropy studies of the cosmic microwave background (CMB) and the discovery of distant massive galaxy clusters through the thermal Sunyaev–Zeldovich (SZ) effect (Sunyaev & Zeldovich 1972). The 840 bolometers are split

Table 1
Flux Densities of SPT Sources

ID	R.A.	Decl.	$S_{350\mu\text{m}}$ (mJy)	$S_{870\mu\text{m}}$ (mJy)	$S_{1.4\text{ mm}}$ (mJy)	$S_{2.0\text{ mm}}$ (mJy)
SPT-S J051259–5935.6	05:12:57.8	−59:35:39.6	223 ± 95	92 ± 12	22.7 ± 3.9	5.5 ± 1.1
SPT-S J052903–5436.6	05:29:03.0	−54:36:33.3	409 ± 35 ^a	112 ± 11	35.4 ± 4.8	9.2 ± 1.3
SPT-S J053250–5047.1	05:32:50.9	−50:47:10.0	353 ± 47	127 ± 10	40.8 ± 5.2	13.4 ± 1.4
SPT-S J053816–5030.8	05:38:16.5	−50:30:52.5	336 ± 88	125 ± 7	29.7 ± 4.6	8.5 ± 1.4
SPT-S J055002–5356.6	05:50:00.5	−53:56:41.2	35 ± 40 ^b	59 ± 10	17.3 ± 4.3	3.9 ± 1.0
SPT-S J055138–5057.9	05:51:39.2	−50:57:59.4	165 ± 27	76 ± 11	26.7 ± 4.2	5.0 ± 0.9
SPT-S J231921–5557.9	23:19:21.5	−55:57:57.6	50 ± 10 ^b	41 ± 5	17.5 ± 4.2	5.4 ± 1.2
SPT-S J233227–5358.5	23:32:26.5	−53:58:39.8	425 ± 39 ^c	150 ± 11 ^c	34.4 ± 4.7	... ^d
.....-A	23:32:29.7	−53:58:38.4	148 ± 21 ^e	51 ± 7
.....-B	23:32:27.6	−53:58:42.8	92 ± 21 ^e	38 ± 8
.....-C	23:32:25.8	−53:58:38.0	137 ± 21	43 ± 8
.....-D	23:32:29.0	−53:57:59.0	65 ± 21 ^b	22 ± 4
.....-E	23:32:29.4	−53:59:31.0	39 ± 21 ^b	21 ± 5
.....-F	23:32:27.1	−56:58:17.0	17 ± 21 ^b	18 ± 4
SPT-S J234942–5638.2	23:49:42.3	−56:38:41.2	94 ± 41 ^b	82 ± 8	20.3 ± 4.5	5.0 ± 1.2
.....-A	23:49:43.1	−53:58:17.0	5 ± 41 ^b	28 ± 8
SPT-S J235338–5010.2	23:53:39.9	−50:10:05.2	24 ± 21 ^b	43 ± 6	19.9 ± 4.8	5.8 ± 1.3
SPT-S J235718–5153.7	23:57:17.1	−51:53:52.1	74 ± 39	46 ± 7	19.8 ± 4.6	4.3 ± 1.0

Notes. SABOCA (350 μm) and LABOCA (870 μm) flux densities of the 11 SPT sources presented in this paper, along with their SPT (1.4 and 2.0 mm) flux densities. The positions are the 870 μm centroid positions, except for SPT 2332–53-A, -B, and -C, where the 350 μm centroid positions are used. Unless otherwise stated, all 350 μm fluxes were measured within an aperture corresponding to the LABOCA beam solid angle (see Section 3.2). The errors given are statistical only. For the SED fitting analysis, we add the absolute calibration uncertainty in quadrature to the statistical uncertainty.

^a The flux is integrated within a 25'' aperture covering the extended emission.

^b No 350 μm emission peak at S/N ≥ 3 . The 350 μm flux was measured within an aperture corresponding to the LABOCA beam solid angle (see Section 3.2).

^c The flux is integrated within a 44'' aperture covering the -A, -B, -C, and -F components.

^d No 2.0 mm flux measurements available for this source; see Section 3.2 for details.

^e The flux is measured within a 13'' aperture.

into six wedges each containing 140 detectors. In 2008 (the season during which the SPT data in this work were taken), the array consisted of a single 3.2 mm wedge, three 2.0 mm wedges, and two 1.4 mm wedges. The 3.2 mm wedge did not produce science-quality data, but the 1.4 and 2.0 mm wedges performed to specification, resulting in rms survey depths of approximately 1.3 mJy at 2.0 mm and 3.4 mJy at 1.4 mm. The 10 m primary mirror of the SPT results in beam sizes (FWHM) of approximately 1''.0 at 1.4 mm and 1''.1 at 2.0 mm. The camera was upgraded to provide sensitivity in all three bands for observations starting in 2009. The 2500 deg² SPT-SZ survey was completed in all three bands in 2011 November.

The data reduction pipeline applied to the SPT data is described in Vieira et al. (2010, hereafter V10). Briefly, the SPT time-ordered data from every working detector are calibrated and bandpass filtered, one or more common modes are removed from the data of all the detectors on a given wedge, and the data from all detectors in a given wavelength band are co-added into a map using inverse-noise weighting.

Sources are identified in SPT maps as described in V10. Objects are identified by first convolving the single-band map with a matched filter (e.g., Haehnelt & Tegmark 1996) that de-weights noise and astrophysical signals on large scales and maximizes sensitivity to point-like objects and then searching the filtered map for high-significance peaks. Sources are then cross-matched between the 1.4 and 2.0 mm catalogs, and their fluxes are de-boosted according to the method detailed in Crawford et al. (2010). Sources detected in SPT maps are classified as dust-dominated or synchrotron-dominated based on the ratio of their flux in the 1.4 and 2.0 mm bands. Approximating the spectral behavior of sources between 1.4 and 2.0 mm as a power law, $S(\lambda) \propto \lambda^{-\alpha}$, we estimate the spectral index α for

every source and use $\alpha = 1.66$ as the dividing line between dust- and synchrotron-dominated populations, thereby removing all flat-spectrum radio quasars from the sample (see V10 for details). We apply an additional selection on the sample by imposing a cut on sources found in the Infrared Astronomy Satellite Faint-Source Catalog (IRAS-FSC; Moshir et al. 1992). This corresponds to cutting out sources with $S_{60\mu\text{m}} > 200$ mJy, which should remove any source at $z < 1$ from this sample. Absolute calibration for both the 1.4 and 2.0 mm bands is derived from the CMB, and the calibration uncertainty is $\lesssim 10\%$, as described in Vieira et al. (2010).

For the study presented here, 11 sources from 200 deg² of the 2008 survey data were imaged at 870 and 350 μm . Their 1.4 mm fluxes range from 17 to 40 mJy and approximate a flux-limited sample. The sources are listed with their full source names in Table 1; throughout the paper, we refer to them by their truncated coordinates (e.g., SPT-S J233227–5358.5 becomes SPT 2332–53).

2.2. APEX Submm Continuum Imaging

The submm observations presented in this paper were carried out at 350 and 870 μm with the SABOCA and the LABOCA at the Atacama Pathfinder EXperiment (APEX).³² The sources observed and their coordinates are given in Table 1.

LABOCA is a 295-element bolometer array (Siringo et al. 2009) with an 11''.4 field of view and a measured angular resolution of 19''.7 (FWHM). The center frequency of LABOCA is 345 GHz (870 μm) with a passband FWHM of ~ 60 GHz.

³² APEX is a collaboration between the Max-Planck Institute für Radioastronomie, the European Southern Observatory, and the Onsala Space Observatory.

The measured noise performance for these observations was $60 \text{ mJy s}^{1/2}$.

SABOCA is a 39-element TES bolometer array (Siringo et al. 2010) with a $1.5'$ field of view and a measured angular resolution of $7.8'$ (FWHM). The center frequency of SABOCA is 860 GHz ($350 \mu\text{m}$) with a passband FWHM of ~ 120 GHz. The measured noise performance for these observations was $150 \text{ mJy s}^{1/2}$.

SABOCA and LABOCA observations of seven of our sources were carried out during Max-Planck observing time in 2010 May (PI: Weiß). A further four sources were observed in 2010 August under ESO programs 086.A-1002A and 087.A-0968A (PI: Greve). This brings the total number of sources presented in this paper to 11. All SABOCA observations were obtained in excellent weather conditions (precipitable water vapor, PWV, less than 0.7 mm). The LABOCA $850 \mu\text{m}$ observations of all targets were done in good weather conditions (PWV < 1.5 mm).

Typical integration times for LABOCA were 1 hr on-source resulting in an rms level of $\sim 6 \text{ mJy beam}^{-1}$, adequate to detect any of the SPT sources at $z < 9$, assuming a point-like source (with respect to the LABOCA beam) and an SED similar to other SMGs.

At the time of our observations, we had no information on source redshifts, SED shapes, or resolved structure, all of which can dramatically vary the expected $350 \mu\text{m}$ flux density for a given 1.4 mm flux density. The SABOCA observations therefore targeted a fixed rms of 30 mJy beam^{-1} (~ 3 hr on-source). At this noise level we expected a 5σ detection for a typical redshift of $z \sim 3$, assuming an unresolved point source. For sources that were not detected at this noise level we increased the integration time up to 5 hr on-source, yielding an rms of $\sim 20 \text{ mJy beam}^{-1}$, which should detect a typical source out to approximately $z \sim 4$.

Mapping was performed using the raster–spiral mode (Siringo et al. 2009) for both bolometer arrays. This mode yields map sizes slightly larger than the field of view of the arrays ($\approx 1.5'$ and $12'$ for SABOCA and LABOCA, respectively). The SABOCA maps are thus well matched to the SPT resolution (FWHM $\sim 1'$) and positional uncertainty of the SPT source (rms $\sim 10''$).

Calibration was achieved through observations of Mars, Uranus, and Neptune, as well as secondary calibrators, and was found to be accurate within 10% and 25% at 870 and $350 \mu\text{m}$, respectively. The atmospheric attenuation was determined via skydips every ~ 1 – 2 hr, as well as from independent data from the APEX radiometer that measure the line-of-sight water vapor column every minute. Focus settings were determined typically once per night and checked during sunrise. Pointing was checked on nearby quasars and found to be stable within $3''$ rms.

The data were reduced using the Bolometer Array analysis software (BoA) reduction package (Schuller et al. 2010). The time-ordered data undergo flat fielding, calibration, opacity correction, correlated noise removal on the full array and on groups of bolometers related by the wiring and in the electronics, flagging of unsuitable data (bad bolometers and/or data taken outside reasonable telescope scanning velocity and acceleration limits), and de-spiking. Each reduced scan was then gridded into a spatial intensity and weighting map. Weights are calculated based on the rms of each time series contributing to a certain grid point in the map. Individual maps were co-added with inverse variance weighting. The resulting map was used in a second iteration of the reduction to flag those parts of the time streams with significant source signal. This guarantees that the source fluxes are not affected by filtering and baseline subtraction. For

sources that remained undetected at $350 \mu\text{m}$, we flagged a region with $15''$ radius centered on the $870 \mu\text{m}$ LABOCA position in the $350 \mu\text{m}$ time streams.

2.3. *Spitzer*-IRAC Imaging

Mid-infrared *Spitzer*/Infrared Array Camera (IRAC) imaging was obtained on 2009 August 2 as part of a larger *Spitzer* program (PID 60194; PI Vieira) to follow up bright submm galaxies identified in the SPT survey. The on-target observations consisted of 36×100 s and 12×30 s dithered exposures at 3.6 and $4.5 \mu\text{m}$, respectively. A large dither pattern was used for the $3.6 \mu\text{m}$ exposures, and a medium dither pattern was used at $4.5 \mu\text{m}$. This scheme was designed to provide $3.6 \mu\text{m}$ imaging sufficiently deep to detect even very distant galaxies, while also providing a minimal level of sensitivity at $4.5 \mu\text{m}$ to furnish infrared colors for low-redshift sources nearby.

The data were reduced following the methods described in Ashby et al. (2009). The corrected Basic Calibrated Data (cBCD) frames were modified individually to eliminate column pull-down artifacts and treated to remove residual images arising from prior observations of bright sources. The resulting pre-processed frames were then mosaicked with standard outlier rejection techniques using MOPEX under the control of IRACproc (Schuster et al. 2006) to create two mosaics covering the field. The final mosaics were generated with $0.86''$ pixels, i.e., pixels subtending a solid angle equal to half that of the native IRAC pixels. The field covered with at least $10 3.6 \mu\text{m}$ exposures is roughly $6'$ wide, centered on the SPT position. In this work, we show only the $3.6 \mu\text{m}$ images.

2.4. Spectroscopic Redshifts

To date, spectroscopic redshifts have been obtained for two sources in this sample. SPT 0538–50 has a redshift of $z = 2.783$, derived from ionized silicon (Si IV $\lambda 1400$) emission in an optical spectrum with Very Large Telescope (VLT)/X-SHOOTER (284.A-5029; PI: Chapman) and carbon monoxide CO(7–6) and CO(8–7) with APEX/Z-Spec (086.A-0793 and 087.A-0815; PI: De Breuck; and 086.F-9318 and 087.F-9320; PI: Greve). Multiple source images surrounding a low-redshift elliptical galaxy are resolved in high-resolution $890 \mu\text{m}$ imaging with the Submillimeter Array (SMA) (2009A-S076; PI: Marrone). The foreground lens has a measured spectroscopic redshift of $z = 0.443$. A paper detailing these measurements and providing detailed characterization of this source (including lens modeling) is in preparation (D. P. Marrone et al. 2012, in preparation).

SPT 2332–53 has a redshift of $z = 2.738$, derived from Ly α and ionized carbon (C IV $\lambda 1549$) in an optical spectrum with VLT/FORS2 from program 285.A–5034 (PI: Chapman) and carbon monoxide CO(7–6) with APEX/Z-Spec. The redshift of the foreground lens, which is a cluster of galaxies, is $z = 0.403$. A paper providing a full characterization of this source, including unambiguous evidence for it being lensed by the cluster of galaxies, is in preparation (J. D. Vieira et al. 2012, in preparation).

3. RESULTS

3.1. Submillimeter Maps and Source Morphology

Figure 1 shows *Spitzer*/IRAC $3.6 \mu\text{m}$ postage-stamp images of our 11 sources, with the SPT 1.4 mm, LABOCA $870 \mu\text{m}$,

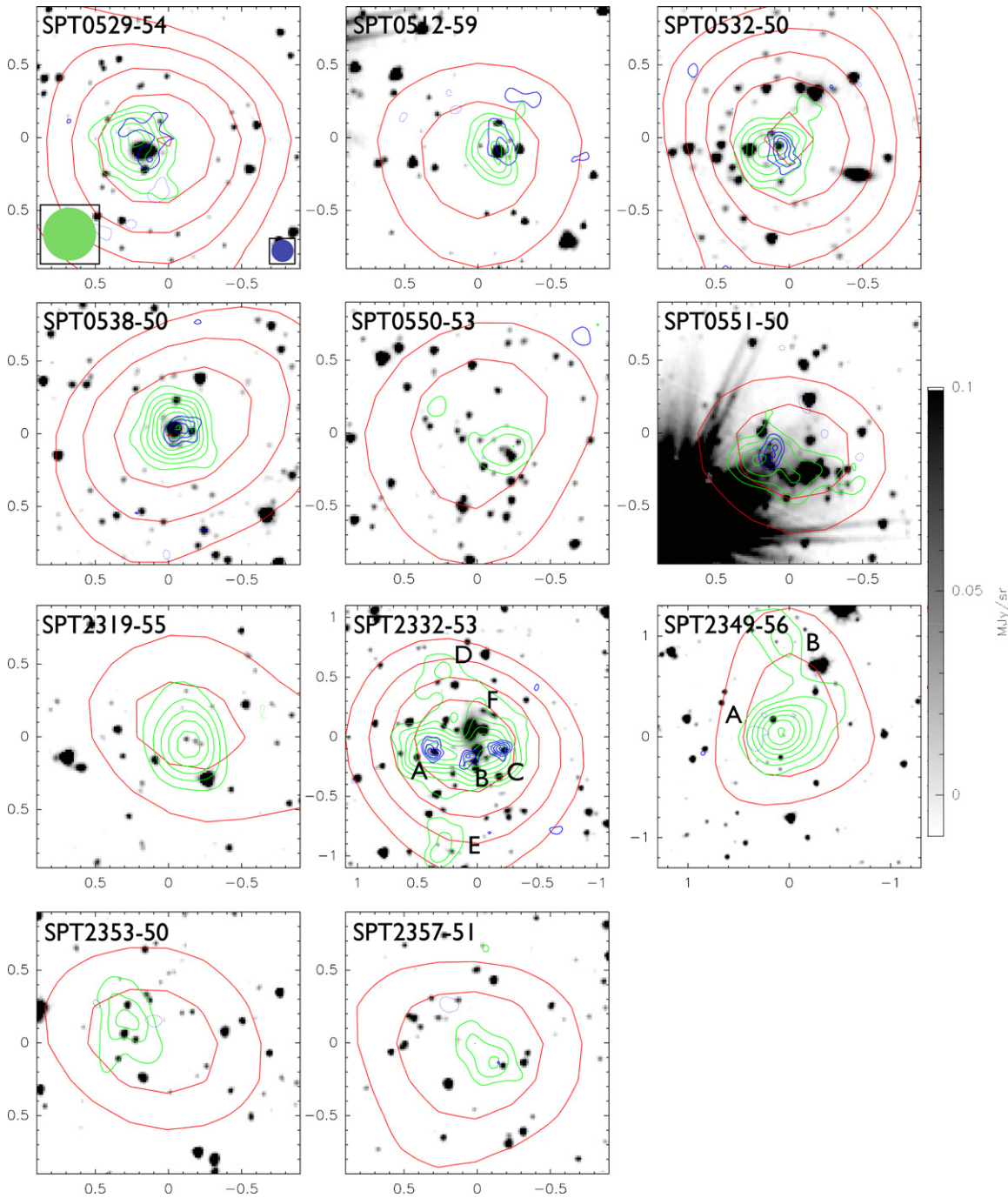


Figure 1. *Spitzer*/IRAC 3.6 μm images (gray scale; $1'8 \times 1'8$ for most, $2'2 \times 2'2$ and $2'6 \times 2'6$ in the cases of SPT 2332–53 and SPT 2349–56, respectively) of the 11 SPT sources presented here, with the corresponding SPT 1.4 mm S/N contours overlaid (red contours), shown at 3, 5, 7, etc. Also overlaid are the same S/N levels (including S/N = –3 shown as dashed contours) for the LABOCA 870 μm (green contours) and SABOCA 350 μm observations (blue contours). The regions shown are centered on the SPT centroid position. The LABOCA and SABOCA beam sizes are represented in the lower left and right corners of the top left panel, respectively.

and SABOCA 350 μm signal-to-noise ratio (S/N) contours overlaid.

All sources are detected at 870 μm at S/N > 6. For 6 of the 11 sources, S/N > 3 in the SABOCA 350 μm images near the LABOCA positions (Figure 1). A further source (SPT 2357–51) is marginally detected at 350 μm as it shows an S/N \simeq 3 emission peak at the LABOCA centroid position. Of the remaining four sources, two (SPT 2349–56 and SPT 2319–55) are tentatively detected (S/N \simeq 2.5) in the SABOCA map, while two show no signs of a SABOCA detection.

All sources, with the exception of SPT 0529–54 and SPT 2332–53, are consistent with being point sources in both the LABOCA and SABOCA maps. Two LABOCA sources are associated with SPT 2349–56 (A and B; see Figure 1), each of which is consistent with a point source. Inserting point sources into the bolometer time streams and subjecting them to the same reduction steps as detailed in Section 2.2 reproduces the observed maps very well.

SPT 0529–54 appears to be resolved at 350 μm , with S/N \sim 3–4 emission extending to the north and east. This

three-component substructure is enclosed within the area of a LABOCA beam, and the source appears point-like at 870 μm .

For SPT 2332–53 the LABOCA 870 μm emission is clearly extended in the east–west direction, spanning $\sim 1'$. At 350 μm the source resolves into three separate, unresolved blobs. We denote these sources A, B, and C, going from east to west (see Figure 1). Two additional sources (D and E) are seen in the LABOCA map to the north and south of the central east–west source. Subtracting point sources at the A, B, and C positions in the LABOCA map reveals an additional LABOCA source, denoted F in Figure 1. While D, E, and F are significant ($\gtrsim 5\sigma$ – 6σ) at 870 μm , no associated emission is seen in the SABOCA map. For a detailed analysis of the properties of SPT 2332–53, we refer to J. D. Vieira et al. (2012, in preparation).

3.2. Millimeter and Submillimeter Fluxes

The LABOCA source coordinates, the SPT flux densities at 1.4 and 2.0 mm, and the LABOCA/SABOCA flux densities at 870 and 350 μm for our 11 sources are listed in Table 1. The SPT flux densities have been determined using the method described in V10. We report the peak flux densities, as none of the sources are resolved in the SPT maps. Submm flux density determinations are discussed below. For all source fitting, the absolute calibration error was added in quadrature to the statistical error.

We do not report the 2.0 mm flux of SPT 2332–53 since it coincides with a massive cluster of galaxies (see Vanderlinde et al. 2010), and the SZ decrement of the cluster at this wavelength overwhelms any emission (J. D. Vieira et al. 2012, in preparation). In the case of SPT 2349–56, we disregard the B component and attribute the SPT 1.4 and 2.0 mm fluxes to component A, which coincides with the SPT centroid.

The 870 μm LABOCA flux densities were determined by fitting a Gaussian with $\text{FWHM} = 21''$, the resolution of the smoothed maps, to the sources (except for SPT 2332–53; see below). A constant baseline term was included in the fit in order to account for any background level.

The 350 μm SABOCA fluxes were derived by summing the flux within an aperture corresponding to the LABOCA beam solid angle ($\Omega = 1.133 \times \text{FWHM}^2$), i.e., within a radius of $r_{\text{ap}} = \sqrt{\Omega/\pi}$. A background level was estimated from a surrounding annular region (inner and outer radii of $r_1 = r_{\text{ap}}$ and $r_2 = \sqrt{2} \times r_{\text{ap}}$) and removed. The aperture was centered on the 870 μm LABOCA centroid. The flux uncertainties were estimated for each source by measuring the flux within the same aperture at the same position in 100 difference maps generated from individual observations and measuring the variance of the resulting distribution. For the SABOCA detections, we compared fluxes obtained by centering the aperture on the SABOCA and LABOCA centroids and found the differences to be $< 10\%$, well within the photometric uncertainties.

For SPT 2332–53, which is resolved into three sources in the LABOCA map, we derived the total flux within an aperture of $r = 44''$. This aperture encompasses components A, B, C, and F. The same aperture was used to measure the corresponding total flux at 350 μm in the SABOCA map. The 1.4 mm SPT flux contains the combined contribution from all four components and possibly also the D and E sources seen in the LABOCA maps, because of the large SPT beam. For subsequent photometric analysis, we ignore any contribution from the positions of D and E to the total flux because of their

large distance from the detected source. The D and E sources are not consistent with being part of the same lensing configuration as A, B, C, and F. The D and E sources do not have obvious IRAC counterparts. We have investigated the possibility that they are artifacts from the LABOCA data processing, but every test indicates that they are real.

SPT 0529–54 is extended in the SABOCA map, so we determined its 350 μm flux using an aperture with radius 25''.

3.3. Spectral Energy Distributions and Redshifts

The majority of our sources do not have spectroscopic redshifts, which prevents us from determining their dust temperatures and luminosities. Our data are not well suited to photometric redshift measurements that rely on LIRG SED templates (e.g., Silva et al. 1998; Chary & Elbaz 2001), as we do not have data in the MIR and NIR where these templates have strong spectral features. The SED of dusty galaxies is nearly featureless at the spectral resolution of bolometer cameras, thereby hampering simple photometric redshift techniques. The most prominent feature, the frequency of the SED peak, cannot provide a redshift without prior information on the dust temperature, as these quantities are degenerate through the ratio $T_d/(1+z)$ (e.g., Blain et al. 2003). Nonetheless, some success in predicting spectroscopic redshifts of SMGs has been achieved by maximum-likelihood techniques that employ libraries of SED templates of local starbursts and ULIRGs in their analysis (e.g., Artxaga et al. 2007).

To overcome this degeneracy, we have developed a method that uses the distribution of SEDs for sources of known redshift taken from the literature. We assume a simple graybody form for the SED to derive T_d for sources in three samples: (1) unlensed sources at $z > 1$ with 350 μm imaging, (2) lensed sources at $z > 1$ with 350 μm imaging, and (3) SPT sources with known redshifts.

For the unlensed sources, we draw our sample from the following:

1. Sixteen sources from Kovács et al. (2006), an 850 μm selected sample with 1.4 GHz radio counterparts, optical spectroscopic redshifts, and 350 μm imaging from CSO/SHARC-II.³³
2. Eleven sources from Kovács et al. (2010), a $z \sim 2$ *Spitzer* IRAC- and MIPS-selected sample with *Spitzer*/IRS MIR spectroscopy, IRAM/MAMBO 1.2 mm imaging, and 350 μm imaging from CSO/SHARC-II.
3. Eighteen sources from Chapman et al. (2010), a 1.4 GHz radio-selected sample with 850 μm detections, optical spectroscopic redshifts, and 250, 350, and 500 μm imaging from *Herschel*/SPIRE.
4. Thirteen optically and radio-selected active galactic nuclei (AGNs) from other studies (Benford et al. 1999; Beelen et al. 2006; Wang et al. 2008, 2010) with optical spectroscopic redshifts, millimeter photometry, and 350 μm imaging from CSO/SHARC-II.

For the lensed sources, we draw our sample from the following:

1. Five well-studied lensed sources from the literature (e.g., Blain 1999; Benford et al. 1999; Barvainis & Ivison 2002), including IRAS F10214+4724, APM 08279+5255, and H1413+117 (the Cloverleaf). The 350 μm imaging for these sources comes from CSO/SHARC-II (Benford et al. 1999;

³³ Some of these sources also have 1.1 mm photometry from CSO/BOLOCAM and/or 1.2 mm photometry from IRAM/MAMBO, which we use, when available.

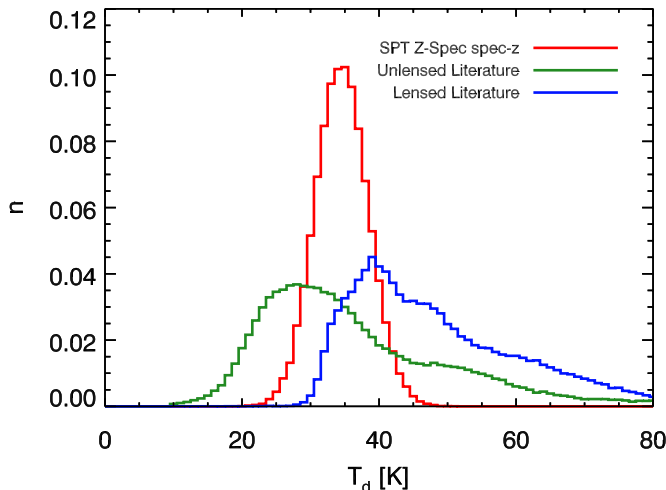


Figure 2. Comparison of the dust temperature distributions derived from calibration samples of (red) two spectroscopically confirmed SPT sources, (blue) all *lensed* high- z sources in the literature with $350\text{ }\mu\text{m}$ detections and spectroscopic redshifts, and (green) *unlensed* $350\text{ }\mu\text{m}$ detected SMGs with spectroscopic redshifts. These distributions are used as priors on T_{d} for our photometric redshift technique, with the unlensed (green) being the primary choice for subsequent analyses. The error bars include the statistical and absolute calibration uncertainties.

Beelen et al. 2006) and millimeter photometry from a variety of literature sources.

2. Two strongly lensed sources discovered behind massive galaxy clusters (the Eyelash and the Bullet) and imaged with SPIRE (Ivison et al. 2010; Rex et al. 2010).
3. Seven lensed sources discovered serendipitously in large extragalactic *Herschel*/SPIRE surveys (Negrello et al. 2010; Omont et al. 2011; Cox et al. 2011; Conley et al. 2011).

For the two SPT sources, we use the measured spectroscopic redshifts described in Section 2.4.

We fit each source in each sample with a blackbody law, modified with a spectral emissivity that varies physically such that the dust opacity reaches unity at frequency ν_c (e.g., Blain et al. 2003):

$$f_{\nu} \propto [1 - \exp(-(\nu/\nu_c)^{\beta})]B_{\nu}(T_{\text{d}}). \quad (1)$$

Here, $B_{\nu}(T_{\text{d}})$ is the Planck function. We fix the spectral index of the emissivity to $\beta = 2.0$ and critical frequency to $\nu_c \simeq 3000\text{ GHz}$ ($\lambda_c \simeq 100\text{ }\mu\text{m}$) following Draine (2006). From these fits, we derive a distribution of dust temperatures for each sample from the sum of the probability distributions of the individual sources (Figure 2). The SED fits exclude any data at wavelengths shorter than $\lambda_{\text{obs}} < 250\text{ }\mu\text{m}$ (rest wavelength $\sim 50\text{ }\mu\text{m}$ for the highest redshift sources) to ensure similarity between the calibration samples and the data in hand for SPT sources in this work. Moreover, such a constraint is appropriate to ensure the applicability of our simple model, which cannot adequately represent emission from hot components that may become apparent at shorter wavelengths. We find that our simple graybody fits all sources well over this wavelength range. We attribute the difference in the dust temperature distributions between the lensed and unlensed sources to the former being selected near the peak of their dust emission (e.g., by SPIRE at $350\text{ }\mu\text{m}$ or, in the case of the bright AGN, by *IRAS* at

$60/100\text{ }\mu\text{m}$), which will bias the selection toward hotter (and more luminous) sources. The unlensed sources were selected from either mm, radio, or IRAC data, and we intentionally marginalized over these three selection techniques to mitigate any bias.

The distribution of T_{d} , apparent L_{FIR} , and z for the three samples can be seen in Figure 3. The lensed sources have the highest apparent luminosity at a given T_{d} , as expected from the gravitational magnification, which increases the solid angle they subtend. The lensed sources appear to be offset in the L_{FIR} versus T_{d} space, indicative of them being randomly sampled from the background and made more luminous by gravitational magnification. The lensed sources pulled from the literature are significantly hotter than the unlensed population. This is presumably due to selection effects.

The detection limits for the types of observations used in the three samples are also shown in the right panel of Figure 3, for the SED model employed in this work and assuming a dust temperature of 35 K . The apparent luminosity threshold decreases at high redshift for SPT selection, owing to the steep rise in the submm SED of these objects for $\beta = 2$.

The observed submm/mm SEDs of the SPT sources are shown in Figure 4. In all cases, the $350\text{ }\mu\text{m}$ data point falls below the power-law extrapolation of the longer wavelength data, giving the photometric redshift technique a spectral feature from which to impose its constraint. To infer a photometric redshift for an SPT source, we compare our data to the modified blackbody SED model described above. We randomly draw a value of T_{d} from one of our distributions and fit the redshift for the SED described by this temperature. Repeating this 10^4 times, we generate a probability distribution for the source redshift that marginalizes over the T_{d} prior and adopt the median and standard deviation of this distribution as the estimate of the photometric redshift and its uncertainty. The unlensed sample has a median dust temperature of $\sim 34\text{ K}$, while the lensed sample has a median dust temperature of $\sim 46\text{ K}$. We adopt the distribution from the unlensed sources throughout this paper under the assumption that lensing is randomly sampling the underlying unlensed population of sources. This is a conservative choice, since of the three distributions, it results in the lowest redshifts because of the $T_{\text{d}}/(1+z)$ degeneracy. Also, the dust temperatures derived for the two sources with spectroscopic redshifts fall in the middle of the unlensed distribution. The photometric redshifts derived from this analysis are indicated in Figure 4 and Table 2.

As a point of comparison, we also fit each SPT source with redshifted SED templates of Arp 220, M82 (Silva et al. 1998), and the Eyelash (Ivison et al. 2010). The Eyelash SED is modeled using a two-component dust model comprising two modified blackbodies with $T_{\text{d}} = 30$ and 60 K and $\beta = 2$, as described in Ivison et al. (2010). We adopt the redshift for which a given template provided the best fit to the data (global χ^2_{ν} minimum) as the best-estimate photometric redshift (for that template). The photometric redshifts and uncertainties obtained from these three SED templates are shown in Figure 4. Without additional photometry shortward of $350\text{ }\mu\text{m}$, it is difficult to discriminate between different SED templates such as Arp 220 or M82. These galaxy template redshifts are consistent with the temperature-marginalized graybody values.

For the two sources with spectroscopic redshifts (SPT 2332–53 and SPT 0538–50), we can also directly check the photometric redshift estimates. In both cases, we recover the true redshift to within the statistical uncertainties.

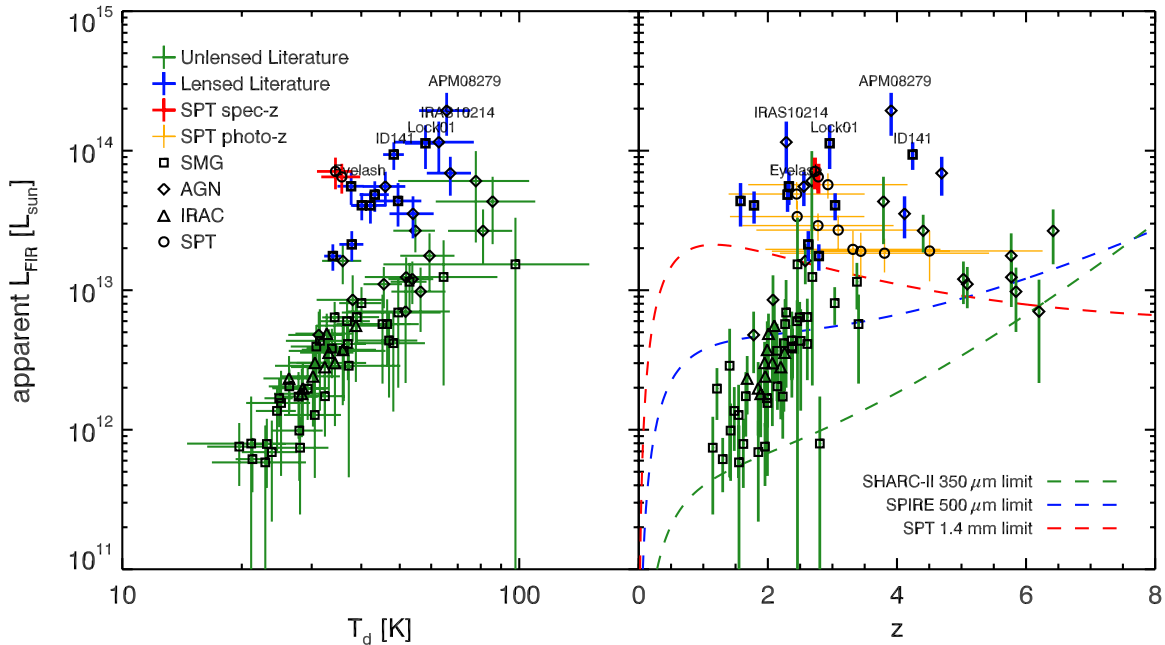


Figure 3. Left: apparent L_{FIR} vs. T_d for all unlensed (green symbols) and lensed (blue symbols) 350 μm detected SMGs and AGNs (squares and diamonds, respectively) with spectroscopic redshifts at $z > 1$ (see Section 3.3 for references). Apparent (i.e., lensed) FIR luminosities vs. dust temperature for the two SPT sources with spectroscopic redshifts presented in this paper (red symbols). For all sources, the FIR luminosities and dust temperatures were derived by fitting a modified blackbody law with $\beta = 2.0$ becoming optically thick at $\lambda_c < 100 \mu\text{m}$. Right: the FIR luminosity as a function of redshift for the same sources. The nine SPT sources presented here that lack spectroscopic redshifts are also plotted (black dots with yellow error bars) with their photometric redshift estimates and associated uncertainties. The uncertainty on L_{FIR} given the assumed photometric redshift is described in Section 3.3, which assumes $T_d = 34 \text{ K}$ —the median dust temperature of the unlensed population. The green, blue, and red dashed curves show the limiting FIR luminosity as a function of redshift corresponding to the effective SHARC-II 350 μm survey limit ($\text{rms} \sim 5 \text{ mJy}$), three times the SPIRE 500 μm confusion limit (30 mJy), and the 3 σ SPT 2.0 mm survey limit (3.9 mJy), respectively, given the SED model of this paper and assuming a 35 K dust temperature. The SPT survey, with its longer wavelength selection, is more sensitive to sources at the highest redshifts ($z > 5$) than *Herschel*, and the large survey area of SPT makes it sensitive to sources that are among the most rare and most highly magnified.

Table 2
Redshifts and Modeled FIR Properties of SPT Sources

Short ID ^a	Photo- z	Spec- z ^b	$L_{\text{FIR}}[8-1000 \mu\text{m}]$ ($\times 10^{13} L_{\odot} \mu^{-1}$)	SFR ($\times 10^3 M_{\odot} \text{yr}^{-1} \mu^{-1}$)	T_d (K)	M_d ($\times 10^{10} M_{\odot} \mu^{-1}$)
SPT 0512–59	2.5 ± 1.0	...	3.4 ± 1.0	5.1 ± 1.2	...	1.0 ± 0.5
SPT 0529–54	2.4 ± 1.1	...	4.9 ± 1.1	7.3 ± 0.7	...	1.3 ± 0.3
SPT 0532–50	2.9 ± 1.2	...	5.7 ± 1.2	8.5 ± 1.6	...	1.4 ± 0.4
SPT 0538–50	2.5 ± 1.0	2.783	6.5 ± 1.6	9.7 ± 1.5	34 ± 3	1.1 ± 0.2
SPT 0550–53	3.4 ± 1.4	...	1.9 ± 0.7	2.8 ± 1.0	...	0.6 ± 0.5
SPT 0551–50	2.8 ± 1.2	...	2.9 ± 0.6	4.3 ± 0.6	...	0.8 ± 0.2
SPT 2319–55	3.8 ± 1.6	...	1.8 ± 0.5	2.7 ± 0.6	...	0.4 ± 0.1
SPT 2332–53	2.5 ± 1.1	2.738	6.5 ± 1.6	9.7 ± 1.3	36 ± 3	1.4 ± 0.3
SPT 2349–56	3.1 ± 1.3	...	2.7 ± 0.7	4.0 ± 1.0	...	0.9 ± 0.5
SPT 2353–50	4.5 ± 1.8	...	1.9 ± 0.8	2.8 ± 1.2	...	0.4 ± 0.2
SPT 2357–51	3.3 ± 1.4	...	2.0 ± 0.7	3.0 ± 0.9	...	0.5 ± 0.7

Notes. Best estimates of dust temperatures, spectral indices, and dust masses as derived from the modified blackbody fits (see Section 3.3). The FIR luminosities, star formation rates, and dust masses are apparent and have *not* been corrected for gravitational amplification, μ , and should therefore be considered strict upper limits. For the sources with only photometric redshifts, the errors of the FIR luminosities, star formation rates, and dust masses have been derived assuming $T_d = 34 \text{ K}$.

^a Shortened source names used throughout the text, with truncated coordinates. Sources are listed in the same order as in Table 1.

^b Spectroscopic redshift derived from VLT spectroscopic observations in the rest-frame UV, and CO line observations with Z-Spec. For these sources, we adopt the spectroscopic redshift when calculating the L_{FIR} , SFR, T_d , and M_d .

3.4. FIR Luminosities, Star Formation Rates, and Dust Masses

Adopting the photometric redshifts and SED fits described in Section 3.3, we can derive FIR luminosities, star formation rates, and dust masses. The fits are shown as black curves in Figure 4 and are seen to provide a good match to the data.

For the two sources with spectroscopic redshifts, we can break the $T_d/(1+z)$ degeneracy and derive the FIR luminosities, star formation rates, and dust temperatures, which are listed in Table 2. For the remaining sources, we derive FIR luminosities, star formation rates, and dust masses by fixing the dust temperature at the median of the distribution for the unlensed sources ($T_d = 34 \text{ K}$).

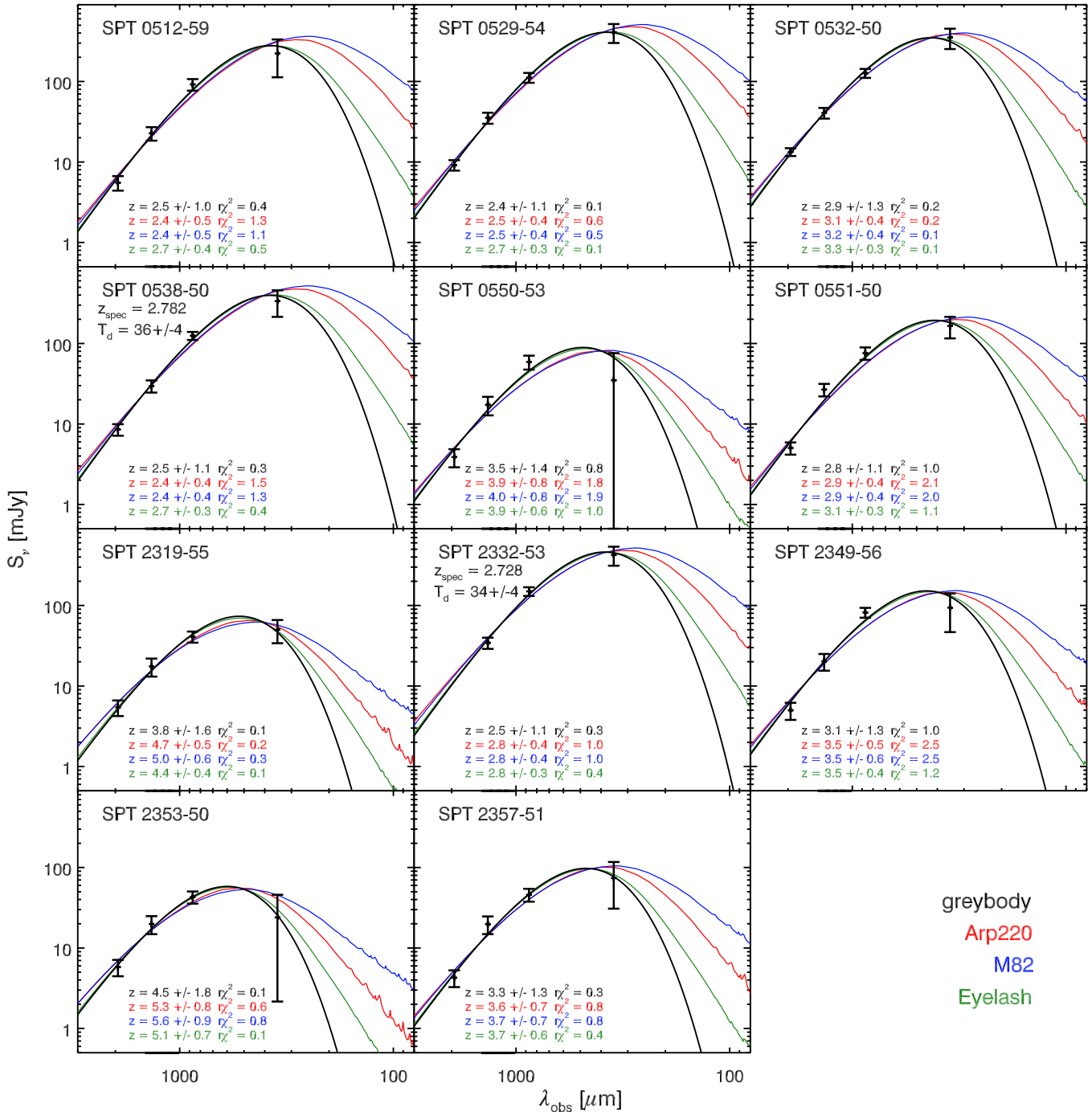


Figure 4. Observed submm/mm SEDs for the 11 sources presented here. The black symbols are SABOCA (350 μm) data, LABOCA (870 μm) data, and SPT photometry (1.4 and 2.0 mm). The black curves are modified blackbody fits with fixed spectral index ($\beta = 2.0$) and $T_{\text{d}} = 34$ K taken from the median value of the unlensed sample of SMGs. Spectroscopic redshifts break the $T_{\text{d}}/(1+z)$ degeneracy (Blain et al. 2003), and in those cases we quote the best-fit dust temperature. The red, blue, and green curves represent the best-fit SEDs to the data based on the Arp 220, M82, and Eyelash SED templates, respectively (see Section 3.3), where the absolute scaling and the redshift have been allowed to vary (the latter is given in each panel). The graybody fit in black is the simplest curve that fits the data. Without additional photometry shortward of 350 μm , it is difficult to discriminate between different SED templates such as Arp 220 or M82.

We determine dust masses according to

$$M_{\text{d}} = \mu^{-1} \frac{D_{\text{L}}^2 S_{\nu_0}}{(1+z)\kappa_{\nu_r}} [B_{\nu_r}(T_{\text{d}}) - B_{\nu_r}(T_{\text{CMB}}(z))]^{-1}, \quad (2)$$

where S_{ν_0} is the flux density at the observed frequency $\nu_0 = \nu_r(1+z)^{-1}$ (which we here set to 345 GHz, the rough central frequency of the LABOCA bandpass). D_{L} is the luminosity distance, μ is the magnification factor, and $T_{\text{CMB}}(z)$ is the CMB

temperature at redshift z (which, in principle, has to be included, although it only changes the dust mass at the $\sim 2\%$ level; Papadopoulos et al. 2000). We adopt $\kappa_{\nu_r}/\text{m}^2 \text{kg}^{-1} = 0.045 \times (\nu_r/250 \text{GHz})^{\beta}$ (Hildebrand 1983; Kruegel & Siebenmorgen 1994), where $\beta = 2.0$ is the adopted dust emissivity index (see Section 3.3). The dust masses (before correcting downward for the unknown magnification) are in the range $M_{\text{d}} \sim (0.4\text{--}1.4) \times 10^{10} M_{\odot}$ (Table 2). We note that significant

uncertainties are associated with these estimates due to the uncertainties in the dust emissivity.

The apparent FIR luminosity is determined from the modified blackbody SEDs, assuming $T_d = 34$ K, as described in Section 3.3. The SED is integrated over the rest wavelength range 8–1000 μm . This yields apparent FIR luminosities in the range $L_{\text{FIR}} \sim (1.8\text{--}6.5) \times 10^{13} L_\odot$ (Table 2). To derive total star formation rates, we use the following conversion from Murphy et al. (2011):

$$\frac{\text{SFR}}{M_\odot \text{ yr}^{-1}} = 1.49 \times 10^{-10} \mu^{-1} \frac{L_{\text{FIR}}[8\text{--}1000 \mu\text{m}]}{L_\odot}. \quad (3)$$

The resulting apparent star formation rates are in the range $\sim(2.7\text{--}9.7) \times 10^3 M_\odot \text{ yr}^{-1}$ (Table 2). No correction has been applied to L_{FIR} or the star formation rate for the unknown gravitational magnification factor, and we use the factor of μ to indicate that these values are upper limits. Even if the lensing correction was known, we have assumed that AGNs do not contribute significantly to the FIR luminosity, and the star formation rates would therefore still be upper limits.

Assuming a gas-to-dust mass ratio of ~ 100 , consistent with what is found for normal SMGs (e.g., Santini et al. 2010), we infer total apparent gas masses in the range $M_{\text{gas}} \sim (0.4\text{--}1.4) \times 10^{12} M_\odot$ and gas-depletion timescales of $t_{\text{depl}} \sim M_{\text{gas}}/\text{SFR} \sim 100\text{--}220$ Myr. This is consistent with the lower limit gas-depletion timescales ($t_{\text{depl}} > 40$ Myr) inferred from CO observations of normal SMGs (Greve et al. 2005). Note that the gas-depletion timescale estimate is independent of the lensing amplification factor as it enters in both the estimate of total gas mass and the star formation rate.

4. DISCUSSION

4.1. FIR Luminosities and Dust Temperatures

In this section, we compare the derived properties of our SPT sources with those of other ultra-bright SMGs from the literature with 350 μm measurements and spectroscopic redshifts of $z > 1$. This comparison is summarized in Figure 3, which shows L_{FIR} versus z and T_d versus L_{FIR} for the SPT sources and other ultra-bright SMGs, normal SMGs, and AGNs.

As can be seen in Figure 3, where we plot L_{FIR} versus T_d , the two SPT sources with spectroscopic redshifts (and thus well-determined dust temperatures) are significantly cooler than other lensed, ultra-bright sources with similar FIR luminosities. The dust temperatures (determined using the SED fit described in Section 3.3) of the strongly lensed sources from the literature are in the range $T_d = 34\text{--}67$ K with a median of 46 K, while the SPT dust temperatures have a mean $T_d = 35$ K (see Table 2 and Figure 2). The fact that the SPT sources appear to have lower dust temperatures than other ultra-bright SMGs with similar FIR luminosities is likely due to the shorter wavelength (< 1 mm) selection of the latter, which will be biased toward warmer temperatures. Also, the ultra-bright SMGs (and AGNs) from the literature were selected based on their extreme brightness, which probably implies a preference toward warmer dust temperatures. It is also possible that strong lensing preferentially selects toward compact and warmer objects. Finally, differential magnification may have an effect on the measured source temperatures (e.g., Blain 1999), but it is beyond the scope of this paper to address this issue.

For SPT sources with only photometric redshifts, we infer apparent FIR luminosities (integrated from 8 to 1000 μm) in

the range $\sim(2\text{--}6) \times 10^{13} L_\odot$. In Figure 3 we plot the FIR luminosities as a function of redshift, along with those of the above-mentioned lensed and unlensed SMGs from the literature. The SPT sources have apparent FIR luminosities comparable to those of other lensed, ultra-bright SMGs, such as the SPIRE sources with spectroscopic redshifts, which have apparent FIR luminosities in the range $(3.9\text{--}7.8) \times 10^{13} L_\odot$. In comparison, normal SMGs have an average intrinsic FIR luminosity of $2.5 \times 10^{12} L_\odot$ (with a range $\sim 10^{11}\text{--}3 \times 10^{13} L_\odot$; Kovács et al. 2006). Thus, the apparent luminosities of ultra-bright SMGs (including those discovered by SPT) are typically an order of magnitude higher than those of the normal SMGs. To a large extent, this difference is expected to reflect the lensing amplification of the ultra-bright SMGs. In the case of the Eyelash, where the amplification factor is well known ($\mu = 32$), the intrinsic FIR luminosity obtained after correcting for lensing is $2.3 \times 10^{12} L_\odot$ (Ivison et al. 2010), which is typical of normal SMGs.

4.2. SPT Sources Are Strongly Lensed

High-resolution follow-up observations of extremely bright SMGs in the literature have shown the majority to be strongly lensed, dusty galaxies (Swinbank et al. 2010; Fu et al. 2012). It seems reasonable to assume that the SPT sources, given their similarity to the literature sources, are also highly lensed, although we cannot rule out that some fraction of them are intrinsically extremely luminous.

For some of the SPT sources, there is indeed unequivocal evidence that they are strongly lensed. In the case of SPT 2332–53, the LABOCA source is resolved into three distinct SABOCA sources—a morphology that strongly suggests we are dealing with a single source undergoing strong gravitational lensing. This is confirmed in optical/near-IR imaging of this source, where the SABOCA sources are clearly seen to line up with a giant arc (J. D. Vieira et al. 2012, in preparation). Similarly in SPT 0529–54, the LABOCA source is resolved into an extended SABOCA source with multiple peaks, again indicative of strong lensing. Finally, in at least one other case (SPT 0538–50), we see structure in the submm emission consistent with gravitational lensing (D. P. Marrone et al. 2012, in preparation). A lack of high-resolution (sub)mm imaging prevents us from constructing accurate lens models and deriving the intrinsic properties of the remainder of the sources. The mass scale of the halos responsible for lensing the SPT population (i.e., galaxy-scale lensing, cluster lensing, etc.) is still poorly determined, although theoretical modeling indicates that the majority of the sources should be lensed by massive elliptical galaxies at $z \sim 1$ (Hezaveh & Holder 2011). Future publications will address the lensing statistics for this sample.

The SED fitting performed in Section 3.3 provides a way to estimate the average magnification of the SPT sources. The luminosity and temperature of the sources are related by a version of the Stefan–Boltzmann law, modified to account for the frequency-dependent emissivity of the sources, so that $L_{\text{FIR}} = 4\pi R^2 \sigma T_d^4$, where we assume that the SPT sources emit as modified blackbodies isotropically from a surface of radius R . The effective Stefan–Boltzmann constant, σ_{eff} , is determined for our model by setting $\sigma_{\text{eff}}/\sigma$ equal to the ratio of the integral of the modified blackbody over a perfect Planck blackbody. For our model, with the opacity reaching unity at $\lambda_c = 100 \mu\text{m}$ and $T_d = 34\text{--}36$ K (as for the two SPT SMGs with spectroscopic redshifts), $\sigma_{\text{eff}}/\sigma$ varies from 0.51 to 0.54. Using this relation, we solve for the apparent effective radii obtained

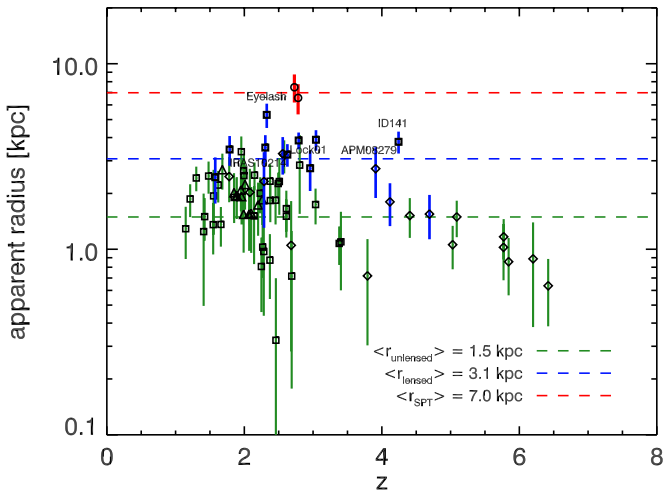


Figure 5. Apparent radius (parameterized as $\propto (L_{\text{FIR}}/T_d^4)^{1/2}$ in units of kpc) of the two SPT sources with spectroscopic redshifts (red symbols). Other strongly lensed sources (SMGs and dusty AGNs: blue symbols) from the literature are also shown, as are the normal, unlensed SMGs (green symbols). In the text we argue that the larger apparent radius of the SPT sources is due to gravitational lensing.

for the SPT sources, and also for the lensed and unlensed SMGs and dusty AGNs from the literature.³⁴ Assuming that the intrinsic sizes and dust temperatures of the SPT sources are, on average, similar to those of the unlensed SMGs, we can ascribe the differences in the apparent radii to different average magnification factors. From Figure 5 we find an average size ratio of $\langle R_{\text{SPT}} \rangle / \langle R_{\text{SMG,unlensed}} \rangle \simeq 4.7$, which translates into a magnification ratio of $\langle \mu_{\text{SPT}} \rangle \sim 22$. We stress that while the apparent size estimates will depend on the optically thick transition wavelength, λ_c , all sources are fitted with the same SED model, and so changing λ_c will not alter the relative trend seen.

For the SPT sources with photometric redshifts, the implied lensing magnification strongly depends on the assumed dust temperature. Sampling the distribution of temperatures associated with the unlensed catalog, we find a broad distribution of magnifications for the SPT photometric sources with 67% of the total samples indicating lensing magnification $\mu > 5$. Fixing the dust temperature for all sources to be $33 \text{ K} < T_d < 35 \text{ K}$, as was found for the two SPT sources with spectroscopic redshifts, we find the mean magnification of the SPT sources with photometric redshifts to be $\bar{\mu} = 11$. In order to make the SPT sample of photometric redshift sources consistent with no lensing $\bar{\mu} \leq 1$, it is necessary for the mean dust temperature to be greater than $T_d > 80 \text{ K}$.

4.3. The Redshifts of Ultra-bright SMGs

From the 11 SPT sources presented in this paper, we find a median redshift of $\bar{z} = 3.0$ with a 68% range of $z = 2.0\text{--}4.6$ using the modified blackbody fits (see Section 3.3). If we instead use the Arp 220, M82, and Eyelash SED templates, we find in all cases median redshifts of $\bar{z} = 3.1\text{--}3.2$. We emphasize that while the photometric redshifts derived in Section 3.3 should

³⁴ For simplicity we have assumed that the modification of the Stefan–Boltzmann law is the same for all sources, given by the value of $T_d = 34 \text{ K}$, the median for the unlensed population. It varies by a factor of $\pm 50\%$ over the 20–50 K range of T_d enclosing the bulk of the unlensed SMGs and asymptotes to unity at large T_d , but factors of order unity are unimportant for this argument.

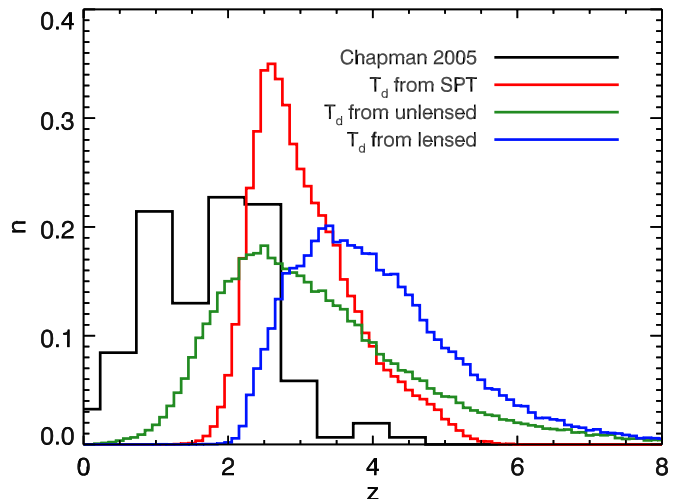


Figure 6. Comparison of our estimated redshift distributions of the SPT sources assuming a T_d distribution derived from (red) the two spectroscopically confirmed SPT sources, (blue) all *lensed* high- z sources in the literature with $350 \mu\text{m}$ detections and spectroscopic redshifts, and (green) *unlensed* $350 \mu\text{m}$ detected SMGs with spectroscopic redshifts. The black solid histogram shows the normalized spectroscopic redshift distribution of normal unlensed $850 \mu\text{m}$ selected SMGs based on an updated version of the Chapman et al. (2005) sample (Banerji et al. 2011) and including the five spectroscopically confirmed normal $z > 4$ SMGs. Note that the black histogram is for individual spectroscopic redshifts, while the colored lines correspond to the probability distributions of photometric redshifts for the SPT sample. All curves have been normalized such that the integral is equal to unity.

not be considered more reliable than within $\Delta z \sim 1$ on a source-by-source basis, our analysis does indicate that when taken as a sample (which includes two spectroscopic redshifts) the SPT sources do have a very high average redshift. The use of the unlensed sample of SMGs as the T_d prior is conservative in that it results in lower redshifts than would be found by using the lensed sample. The agreement between the modified blackbody and template-derived redshift distributions and the comparison to the two SPT sources with spectroscopic redshifts suggest that this assumption is reasonable.

The redshift distribution for the SPT sources is shown in Figure 6 for all three choices of the calibration sample for the modified blackbody fitting technique. The redshifts for a sample of normal, radio-identified, $850 \mu\text{m}$ selected SMGs are also shown ($\bar{z} = 2.2$; Chapman et al. 2005), where we have updated the distribution to include five additional unlensed SMGs spectroscopically confirmed to reside in the redshift range $z = 4.05\text{--}5.3$ (Capak et al. 2008, 2011; Knudsen et al. 2008; Coppin et al. 2010), as well as newly obtained redshifts by Banerji et al. (2011) of SMGs in the spectroscopic “redshift desert” ($z = 0.8\text{--}1.5$). If the SPT sources have similar dust temperatures as the unlensed SMG population at $z > 1$ with spectroscopic redshifts, then the FIR colors imply that the SPT sources are at systematically higher redshifts. For all choices of calibration sample (which provide the T_d prior), the SPT sources are at higher median redshift than the Chapman et al. (2005) sources.

The SPT sources are hypothesized to be a sample of gravitationally magnified members of the normal SMG population, which suggests that they should be drawn from the same redshift distribution. The difference in their observed redshift distributions is likely due to a combination of selection effects. First, the Chapman et al. (2005) sample is strongly selected against high-redshift objects by virtue of the reliance on radio

detections to inform spectroscopic follow-up. Some correction is provided by the addition of newer sources found to be at higher redshift, but the selection remains important. For the SPT sample, we removed any source that is detected in the IRAS-FSC, thereby removing low-redshift unlensed interlopers and possibly a small number of lensed sources at $z \sim 1$. The longer wavelength selection of the SPT sample also admits very high redshift sources that would be harder to detect at $850 \mu\text{m}$ as the SED peak approaches the bolometer passband. Finally, the strong lensing condition itself is expected to introduce a bias toward higher redshift objects. Theoretical work predicts that gravitational magnification by clusters and galaxies shifts the redshift distribution of an observed source population toward higher redshifts than an equivalent field-selected sample (Broadhurst et al. 1995; Blain 1996; Negrello et al. 2007; Jain & Lima 2011).

5. SUMMARY

We have presented SABOCA $350 \mu\text{m}$ and LABOCA $870 \mu\text{m}$ maps and fluxes of 11 ultra-bright SMGs from the SPT survey, resulting in the first FIR/submm SEDs of SPT sources. Employing a novel method, which makes use of a compilation of SEDs of 58 sources with spectroscopic redshifts at $z > 1$ and with $350 \mu\text{m}$ photometry, we have derived photometric redshift estimates for our sources. In the two cases where we have spectroscopic redshifts, they agree well with the photometric redshifts from this analysis. The SPT redshift distribution, with a mean of $\bar{z} = 3.0$ and a 68% confidence region $z = 2.0\text{--}4.6$, is found to be skewed toward significantly higher redshifts than the distribution observed for the normal unlensed SMG population. We argue that the higher mean redshift of the SPT sources is due to the longer selection wavelength and the lensing selection criterion.

Using the median dust temperature measured from the unlensed population of sources from the literature, we fit modified blackbody laws to the observed SPT SEDs and estimated their apparent (i.e., lensing-uncorrected) FIR luminosities ($L_{\text{FIR}} \sim 3.7 \times 10^{13} L_{\odot}$), star formation rates ($\text{SFR} \gtrsim 2500 M_{\odot} \text{ yr}^{-1}$), and dust masses ($M_{\text{d}} \sim (0.4\text{--}1.9) \times 10^{10} M_{\odot}$). Based on the two SPT sources with spectroscopic redshifts, we derive dust temperatures ($\sim 35 \text{ K}$) similar to that of normal SMGs. From the same two sources, we estimate a value of ~ 22 for the gravitational magnification factor. Such a large magnification factor is in line with tentative lens models (J. D. Vieira et al. 2012, in preparation; D. P. Marrone et al. 2012, in preparation) and theoretical modeling (Hezaveh & Holder 2011). Once corrected for lensing, our findings, as well as those of others (e.g., Conley et al. 2011), suggest that the intrinsic properties of the ultra-bright SMGs will fall within the range of normal SMGs. Based on theoretical models and the measured projected area, it appears that the wide field coverage of the SPT finds the rarest, brightest objects, including those with the highest magnification relative to strongly lensed SMGs and AGNs found in the literature.

Due to the extraordinary boosting of the flux and angular size caused by the gravitational lensing, ultra-bright SMGs are ideal targets for high-resolution follow-up observations with the Atacama Large Millimeter Array (ALMA), *Herschel Space Observatory*, and the *Hubble Space Telescope*. These observatories can access the dust properties, gas kinematics, and star formation conditions on sub-kpc scales in these systems. These observations were based on sources selected from 200 deg^2 . SPT has now surveyed 2500 deg^2 , and an extensive multi-wavelength campaign is ongoing.

The authors thank A. Blain and N. Scoville for stimulating discussions and guidance. We are grateful to the competent staff at the APEX base camp in Sequitor, Chile. The South Pole Telescope is supported by the National Science Foundation through grants ANT-0638937 and ANT-0130612. Partial support is also provided by the NSF Physics Frontier Center grant PHY-0114422 to the Kavli Institute of Cosmological Physics at the University of Chicago, the Kavli Foundation, and the Gordon and Betty Moore Foundation. T.R.G. acknowledges support from IDA. The McGill group acknowledges funding from the National Sciences and Engineering Research Council of Canada, Canada Research Chairs program, and the Canadian Institute for Advanced Research. M.D. acknowledges support from an Alfred P. Sloan Research Fellowship. A.A.S. acknowledges support by the Becker Fund of the Smithsonian Institution. This research has made use of the NASA/IPAC Extragalactic Database (NED), which is operated by the Jet Propulsion Laboratory, California Institute of Technology, under contract with the National Aeronautics and Space Administration. Finally, we are grateful to the directors of ESO and the SMA for granting us director's discretionary time.

Facilities: APEX (SABOCA, LABOCA, Z-Spec), *Spitzer*, SPT.

REFERENCES

- Aretxaga, I., Hughes, D. H., Coppin, K., et al. 2007, *MNRAS*, **379**, 1571
- Ashby, M. L. N., Stern, D., Brodwin, M., et al. 2009, *ApJ*, **701**, 428
- Austermann, J. E., Aretxaga, I., Hughes, D. H., et al. 2009, *MNRAS*, **393**, 1573
- Banerji, M., Chapman, S. C., Smail, I., et al. 2011, *MNRAS*, **418**, 1071
- Barger, A. J., Cowie, L. L., Sanders, D. B., et al. 1998, *Nature*, **394**, 248
- Barvainis, R., & Ivison, R. 2002, *ApJ*, **571**, 712
- Beelen, A., Cox, P., Benford, D. J., et al. 2006, *ApJ*, **642**, 694
- Benford, D. J., Cox, P., Omont, A., Phillips, T. G., & McMahon, R. G. 1999, *ApJ*, **518**, L65
- Blain, A. W. 1996, *MNRAS*, **283**, 1340
- Blain, A. W. 1999, *MNRAS*, **304**, 669
- Blain, A. W., Barnard, V. E., & Chapman, S. C. 2003, *MNRAS*, **338**, 733
- Blain, A. W., Moller, O., & Maller, A. H. 1999, *MNRAS*, **303**, 423
- Bradford, C. M., Aguirre, J. E., Aikin, R., et al. 2009, *ApJ*, **705**, 112
- Broadhurst, T. J., Taylor, A. N., & Peacock, J. A. 1995, *ApJ*, **438**, 49
- Capak, P., Carilli, C. L., Lee, N., et al. 2008, *ApJ*, **681**, L53
- Capak, P. L., Riechers, D., Scoville, N. Z., et al. 2011, *Nature*, **470**, 233
- Carlstrom, J. E., Ade, P. A. R., Aird, K. A., et al. 2011, *PASP*, **123**, 568
- Chapman, S. C., Blain, A. W., Smail, I., & Ivison, R. J. 2005, *ApJ*, **622**, 772
- Chapman, S. C., Ivison, R. J., Roseboom, I. G., et al. 2010, *MNRAS*, **409**, L13
- Chary, R., & Elbaz, D. 2001, *ApJ*, **556**, 562
- Conley, A., Cooray, A., Vieira, J. D., et al. 2011, *ApJ*, **732**, L35
- Coppin, K., Chapin, E. L., Mortier, A. M. J., et al. 2006, *MNRAS*, **372**, 1621
- Coppin, K. E. K., Chapman, S. C., Smail, I., et al. 2010, *MNRAS*, **407**, L103
- Cox, P., Krips, M., Neri, R., et al. 2011, *ApJ*, **740**, 63
- Crawford, T. M., Switzer, E. R., Holzapfel, W. L., et al. 2010, *ApJ*, **718**, 513
- Danielson, A. L. R., Swinbank, A. M., Smail, I., et al. 2011, *MNRAS*, **410**, 1687
- Devlin, M. J., Ade, P. A. R., Aretxaga, I., et al. 2009, *Nature*, **458**, 737
- Draine, B. T. 2006, *ApJ*, **636**, 1114
- Eales, S., Dunne, L., Clements, D., et al. 2010, *PASP*, **122**, 499
- Frayer, D. T., Harris, A. I., Baker, A. J., et al. 2011, *ApJ*, **726**, L22
- Fu, H., Jullo, E., Cooray, A., et al. 2012, *ApJ*, **753**, 134
- Gonzalez, A. H., Papovich, C., Bradač, M., & Jones, C. 2010, *ApJ*, **720**, 245
- Greve, T. R., Bertoldi, F., Smail, I., et al. 2005, *MNRAS*, **359**, 1165
- Haehnelt, M. G., & Tegmark, M. 1996, *MNRAS*, **279**, 545
- Harris, A. I., Baker, A. J., Frayer, D. T., et al. 2012, *ApJ*, **752**, 152
- Hezaveh, Y. D., & Holder, G. P. 2011, *ApJ*, **734**, 52
- Hildebrand, R. H. 1983, *QJRAS*, **24**, 267
- Holland, W. S., Robson, E. I., Gear, W. K., et al. 1999, *MNRAS*, **303**, 659
- Hughes, D. H., Serjeant, S., Dunlop, J., et al. 1998, *Nature*, **394**, 241
- Ikarashi, S., Kohno, K., Aguirre, J. E., et al. 2011, *MNRAS*, **415**, 3081
- Ivison, R. J., Swinbank, A. M., Swinney, B., et al. 2010, *A&A*, **518**, L35
- Jain, B., & Lima, M. 2011, *MNRAS*, **411**, 2113
- Johansson, D., Horellou, C., Sommer, M. W., et al. 2010, *A&A*, **514**, A77
- Knudsen, K. K., van der Werf, P. P., & Kneib, J.-P. 2008, *MNRAS*, **384**, 1611

- Kovács, A., Chapman, S. C., Dowell, C. D., et al. 2006, *ApJ*, **650**, 592
 Kovács, A., Omont, A., Beelen, A., et al. 2010, *ApJ*, **717**, 29
 Kruegel, E., & Siebenmorgen, R. 1994, *A&A*, **288**, 929
 Lestrade, J.-F., Combes, F., Salomé, P., et al. 2010, *A&A*, **522**, L4
 Lupu, R. E., Scott, K. S., Aguirre, J. E., et al. 2010, arXiv:1009.5983
 Moshir, M., Kopman, G., & Conrow, T. A. O. (ed.) 1992, IRAS Faint Source Survey, Explanatory Supplement Version 2 (Pasadena, CA: IPAC)
 Murphy, E. J., Condon, J. J., Schinnerer, E., et al. 2011, *ApJ*, **737**, 67
 Negrello, M., Hopwood, R., De Zotti, G., et al. 2010, *Science*, **330**, 800
 Negrello, M., Perrotta, F., González-Nuevo, J., et al. 2007, *MNRAS*, **377**, 1557
 Neri, R., Genzel, R., Ivison, R. J., et al. 2003, *ApJ*, **597**, L113
 Oliver, S. J., Wang, L., Smith, A. J., et al. 2010, *A&A*, **518**, L21
 Omont, A., Neri, R., Cox, P., et al. 2011, *A&A*, **530**, L3
 Papadopoulos, P. P., Röttgering, H. J. A., van der Werf, P. P., et al. 2000, *ApJ*, **528**, 626
 Pascale, E., Ade, P. A. R., Bock, J. J., et al. 2008, *ApJ*, **681**, 400
 Perera, T. A., Chapin, E. L., Austermann, J. E., et al. 2008, *MNRAS*, **391**, 1227
 Rex, M., Rawle, T. D., Egami, E., et al. 2010, *A&A*, **518**, L13
 Santini, P., Maiolino, R., Magnelli, B., et al. 2010, *A&A*, **518**, L154
 Schuller, F., Nord, M., Vlahakis, C., et al. 2010, BoA—The Bolometer Data Analysis Software, User and Reference Manual (http://www.mpifr-bonn.mpg.de/div/submmtech/software/boa_main.html)
 Schuster, M. T., Marengo, M., & Patten, B. M. 2006, *Proc. SPIE*, **6270**, 65
 Silva, L., Granato, G. L., Bressan, A., & Danese, L. 1998, *ApJ*, **509**, 103
 Siringo, G., Kreysa, E., De Breuck, C., et al. 2010, *Messenger*, **139**, 20
 Siringo, G., Kreysa, E., Kovács, A., et al. 2009, *A&A*, **497**, 945
 Smail, I., Ivison, R. J., & Blain, A. W. 1997, *ApJ*, **490**, L5
 Spergel, D. N., Verde, L., Peiris, H. V., et al. 2003, *ApJS*, **148**, 175
 Sunyaev, R. A., & Zeldovich, Y. B. 1972, *Comments Astrophys. Space Phys.*, **4**, 173
 Swinbank, A. M., Smail, I., Longmore, S., et al. 2010, *Nature*, **464**, 733
 Vanderlinde, K., Crawford, T. M., de Haan, T., et al. 2010, *ApJ*, **722**, 1180
 Vieira, J. D., Crawford, T. M., Switzer, E. R., et al. 2010, *ApJ*, **719**, 763
 Wang, R., Carilli, C. L., Neri, R., et al. 2010, *ApJ*, **714**, 699
 Wang, R., Wagg, J., Carilli, C. L., et al. 2008, *AJ*, **135**, 1201
 Weiß, A., Kovács, A., Coppin, K., et al. 2009, *ApJ*, **707**, 1201
 Wilson, G. W., Hughes, D. H., Artxaga, I., et al. 2008, *MNRAS*, **390**, 1061